Journal of Applied Mechanics 93:071006. DOI: 10.1115/1.4071782

Inverse Design of Metamaterials with Adaptable Force-Displacement Characteristics

H. Gökçen Güner,[1,*] Kaushik Dayal,[1,2,3] and Alexandra Ion[4]

[1]*Department of Civil and Environmental Engineering, Carnegie Mellon University*
[2]*Center for Nonlinear Analysis, Department of Mathematical Sciences, Carnegie Mellon University*
[3]*Department of Mechanical Engineering, Carnegie Mellon University*
[4]*Human-Computer Interaction Institute, Carnegie Mellon University*

(Dated: May 21, 2026)

Metamaterials with tailored force-displacement characteristics hold significant promise for applications ranging from soft robotics and energy dissipation to biomedical devices such as prosthetic sockets, where distinct regions of a structure must simultaneously satisfy fundamentally different mechanical requirements. Existing inverse design frameworks, however, are restricted to single loading conditions and homogeneous desired behaviors, limiting their utility in real-world scenarios where complex, spatially varying mechanical demands must be met within a single continuous material. We present an inverse design method that closes this gap by combining finite element simulation, surrogate optimization, and machine learning within a unified framework. Starting from a fixed unit cell topology governed by eleven geometric shape parameters, we first construct a surrogate model that replaces each unit cell with a polynomial energy density, reducing the metamaterial-scale inverse problem to a tractable optimization over polynomial coefficients. A multi-output multilayer perceptron trained on finite element simulations then maps any required unit cell force-displacement response back to the corresponding shape parameters. We extend the formulation to multi-surface loading, enabling two qualitatively distinct force-displacement targets to be achieved simultaneously in different regions of the same structure. Fabricated prototypes tested under prescribed displacements confirm that the predicted responses, spanning superelastic, bistable, and constant-force behaviors, are reproduced with high fidelity. These results demonstrate a flexible and computationally efficient route to multifunctional metamaterial design under realistic, multi-condition loading environments.

1. Introduction

Metamaterials are artificially designed microstructures, which can exhibit varied unusual properties in a single continuous material [IFW$^+$16, PMV15, Sig09, BVCVH17]. By tailoring the design of unit cells, metamaterials can exhibit a diverse range of mechanical behaviors [HWL$^+$23, KZ17], such as nonlinear responses, superelasticity, bistability, and constant-force characteristics [JMR$^+$23, FCvH14, HSSP$^+$16, YM19]. These properties make them ideal for applications such as soft robots [RBS19, PRGM21, MPQF16], energy dissipation systems [YCZ19, SKR$^+$15, ZVLR$^+$21, HLP18], and prosthetics [SGD$^+$19, MJS$^+$18]. In particular, their ability to customize mechanical responses and tunability [FWC$^+$22] under varying loading conditions enables effective solutions for complex environments [SM23, HYX$^+$23, WWC$^+$21, dSDC, ZZLW23]. The force-displacement response is an important indicator of the material's underlying mechanism, providing insights into the material's behavior, including the amount of energy it absorbs and the maximum loads it can sustain [YCZ19, FFK$^+$16].

Inverse design is a key approach in metamaterial research, enabling the optimization of material structures to achieve specific mechanical responses [ZZCW23, KSK$^+$24]. This approach leverages computational simulations to establish relationships between geometry and performance. Advances in machine learning and shape optimization have significantly improved the efficiency of inverse design methods, enabling the rapid prediction and refinement of mechanical behaviors across various conditions. For instance, inverse design techniques have been successfully applied to develop energy-absorbing structures that achieve predefined stress-strain curves, contributing to automotive crash protection and occupant safety systems [ZDZ$^+$23]. Similarly, machine learning models combined with evolutionary strategies have been used to design metamaterials with highly nonlinear responses, facilitating applications such as morphing structures [DZD$^+$22]. However, most existing research primarily focuses on single-loading scenarios, such as pure compression or tension, limiting their applicability to real-world conditions. Since practical applications often involve complex loading environments with multiple simultaneous forces, there is a pressing need for more versatile design frameworks.

To address this limitation, we introduce an inverse design approach that accounts for multiple loading conditions. Our framework optimizes the force-displacement behavior of metamaterials under diverse loading scenarios, enhancing adaptability to real-world applications. By considering different force types and orientations, we aim to develop metamaterials capable of exhibiting multiple functions, including damping, spring-like responses, and force distribution. This is achieved by tuning the shape parameters of unit cells while maintaining the same topology, which enables spatially tailored mechanical responses within a continuous material.

Our methodology begins with the development of a dataset capturing mechanical responses from different unit cell structures, including bistable behaviors, superelasticity, and constant force responses, all governed by unit cell geometry. Because these

* hguner@andrew.cmu.edu

metamaterials undergo large deformations, we employ a hyperelastic material model to ensure accurate characterization. Finite element simulations predict how variations in unit cell shape influence mechanical responses under different loading conditions. Machine learning is then integrated into our design to streamline the inverse design process. By training a multilayer perceptron (MLP) on our simulation results, we rapidly predict unit cell geometries that achieve the desired mechanical responses. Additionally, we develop a surrogate model that simplifies the unit cell's behavior into fundamental geometric elements while preserving its mechanical characteristics. This surrogate model enhances computational efficiency, enabling rapid performance predictions under varying loading conditions.

This work provides a flexible framework for designing multifunctional metamaterials. An application of this approach is in the design of prosthetic sockets, where different regions require distinct mechanical properties. For instance, the tip of a prosthetic socket may need energy absorption to mitigate impact forces during walking, while the lateral regions must maintain a constant grip for stability and comfort. By tailoring metamaterial properties to fulfill these distinct functions simultaneously, we can design prosthetic devices that enhance user comfort and efficiency without the need to assemble multiple materials. To validate our designs, we fabricate the unit cells using 3D printing, allowing us to experimentally assess their performance and compare it with computational predictions.

Finally, our research presents an approach to the inverse design of metamaterials that accounts for multiple loading conditions. By combining computational simulations, machine learning, and 3D printing, we develop adaptable materials with real-world applications. This approach expands the possibilities for advanced material design in biomedical applications, energy dissipation systems, and soft robotics. By optimizing metamaterials for diverse loading scenarios, our work paves the way for more efficient and multifunctional material solutions to complex engineering challenges.

2. Unit Cell Design Space

The inverse design method rests on a characterization of the force-displacement responses that are achievable within a given topology. This section introduces the unit cell geometry, its shape parameters, and the finite element dataset that maps geometry to response. Both the surrogate optimization and the machine learning model described in subsequent sections draw directly from this dataset.

2.A. Topology and Shape Parameters

The unit cell topology is shown in Figure 1. It consists of two interacting curves: an upper curve that governs the primary deformation mechanics under loading, and a lower curve that helps the structure to recover after large deformations. When the configuration promotes snap-through, the unit cell is bistable: it jumps between two stable states, and the lower curve does not push the top curve back. The topology is parameterized by eleven scalar shape parameters, heights h_1 through h_6, widths t_1, t_2, s, and b, and a curvature offset a. These parameters collectively control the geometry of both curves. Varying them within the fixed topology spans the full range of superelastic, bistable, and constant force responses in the dataset.

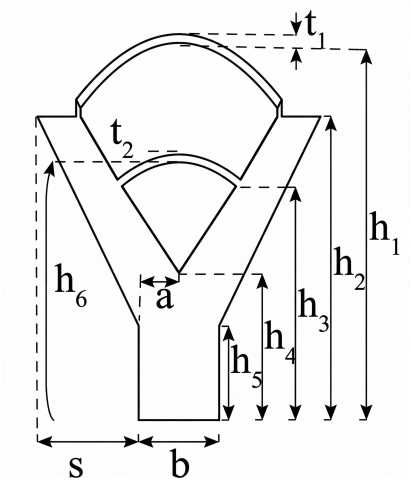

Figure 1. **Unit cell topology and shape parameters.** The unit cell is defined by eleven parameters: heights h_1–h_6, widths t_1, t_2, s, and b, and curvature offset a. These parameters control the geometry of the upper and lower curves. Varying them within the fixed topology produces the full range of superelastic and bistable responses observed in the dataset.

2.B. Finite Element Simulations

To characterize how the eleven shape parameters control the force-displacement response, we performed a large set of finite element simulations using the FEniCS software framework [LMW12]. Each unit cell is modeled with a Neo-Hookean hyperelastic

constitutive law to capture large deformations. Shape parameters were sampled broadly across their feasible ranges. By varying the shape parameters with different combinations, the unit cell was subjected to a full loading-unloading cycle recorded at 50 equally spaced displacement steps, and the resulting force-displacement curve was stored. This process produced a dataset of 10,295 designs. Figure 2 summarizes the dataset through two scalar quantities extracted from each curve: the peak force during loading and the total energy absorbed over one loading-unloading cycle. These two quantities serve as a compact descriptor for each design. The dataset contains 5,552 superelastic designs and 1,384 bistable designs; the remaining designs fall into intermediate categories. Superelastic designs occupy the upper portion of the scatter plot, with higher peak forces and energy absorption, while bistable designs cluster toward the lower end. A trend line with correlation coefficient $r = 0.925$ shows that peak force and energy absorption vary together across the dataset. This correlation reflects the fact that the overall geometry controls both quantities simultaneously, and it means that the design space has a structured geometry that the surrogate optimization can navigate without searching in a brute-force manner.

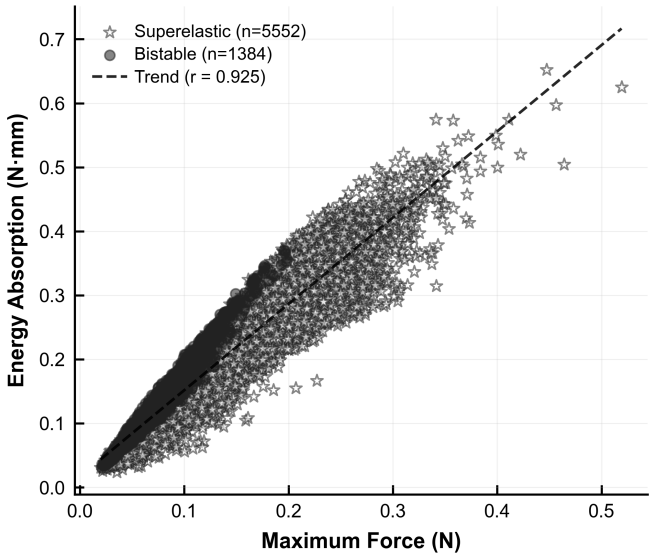

Figure 2. **Dataset overview: peak force and energy absorption across 6,936 classified unit cell designs.** Each point represents a single unit cell design plotted by its peak force (horizontal axis) and energy absorbed per loading-unloading cycle (vertical axis). Superelastic designs (stars, $n = 5{,}552$) occupy the upper portion; bistable designs (circles, $n = 1{,}384$) cluster toward the lower end. A trend line ($r = 0.925$) shows that the two quantities are coupled across the dataset, reflecting the shared geometric origin of both properties.

3. Inverse Design Pipeline

With the dataset established, we can pose the inverse problem. Given a prescribed force-displacement curve for an assembled metamaterial, find the unit cell geometries whose combined mechanical response reproduces the target. In the multi-surface case, there are multiple independent responses, each associated with a different loading surface. The framework proceeds in two sequential stages, illustrated in Figure 3. In the first stage, the metamaterial is replaced by a surrogate model in which each unit cell is represented by a rectangular domain with a polynomial energy density. Optimizing the polynomial coefficients of each domain determines the force-displacement response that each unit cell must produce in terms of a third-order polynomial. In the second stage, a machine learning model maps each required unit cell response back to the eleven shape parameters that generate it. The remainder of this section describes each stage in detail.

3.A. Surrogate Model

Directly simulating a full metamaterial with a complex unit cell geometry is computationally expensive. The surrogate model addresses this by replacing each complex unit cell with a rectangular domain whose behavior is described by a third-order polynomial constitutive response. The polynomial coefficients serve as the decision variables for the optimization. Their allowed range is constrained to remain within the bounds of the finite element dataset, so that every optimized response corresponds to a geometrically realizable design within the unit cell topology. Figure 4 illustrates the surrogate construction for a 2×1 metamaterial. The two physical unit cells are replaced by rectangular domains Ω_1 and Ω_2, each governed by its own polynomial energy density, with a Neo-Hookean layer Ω_3 connecting both to the loading surface.

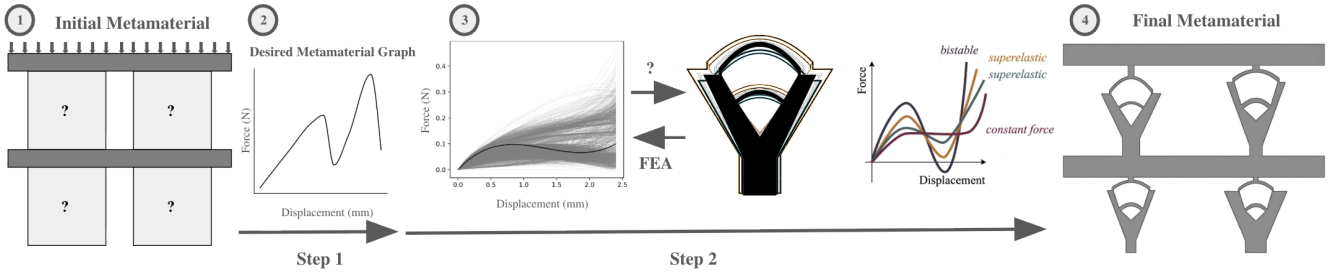

Figure 3. **The inverse design pipeline.** (1) A surrogate model, in which each unit cell is replaced by a polynomial energy density, is optimized to match the target, yielding the required force-displacement behavior of each unit cell. (2) A desired force-displacement curve is specified for the assembled metamaterial. (3) A machine learning model maps each required unit cell response to the eleven shape parameters that produce it, using the finite element dataset. (4) The resulting example unit cell geometries are assembled into the full metamaterial. Arrows show the direction of information flow.

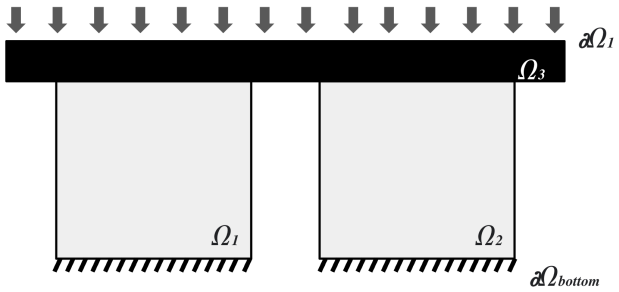

Figure 4. **Surrogate model of a** 2×1 **metamaterial.** The two physical unit cells are replaced by rectangular domains Ω_1 and Ω_2, each governed by a polynomial energy density. A Neo-Hookean layer Ω_3 connects both domains to the prescribed displacement boundary $\partial\Omega_1$ (top, arrows). The fixed bottom boundary $\partial\Omega_{\text{bottom}}$ is indicated by hatching.

a. Governing equations. For a domain $\Omega \subset \mathbb{R}^d$, the displacement field $\boldsymbol{u} : \Omega \to \mathbb{R}^d$ satisfies static equilibrium with prescribed boundary displacements:

$$-\operatorname{div}\big(\boldsymbol{P}(\nabla \boldsymbol{u})\big) = \boldsymbol{0} \quad \text{in } \Omega, \qquad \text{with } \boldsymbol{u} = \boldsymbol{u}_j \text{ on } \partial\Omega_1, \quad \boldsymbol{u} = \boldsymbol{0} \text{ on } \partial\Omega_{\text{bottom}}. \tag{3.1}$$

The equilibrium state minimizes the total potential energy,

$$\min_{\boldsymbol{u}\in V} \Pi, \quad \Pi = \sum_{i=1}^{3} \int_{\Omega_i} \psi_i(\boldsymbol{F})\, d\Omega_i, \tag{3.2}$$

where V is a function space satisfying the displacement boundary conditions.

For the polynomial unit cell domains Ω_1 and Ω_2, the stored energy density is a polynomial in the Green–Lagrange strain component E_{11}:

$$\psi_{1,2} = \frac{a_i}{4}E_{11}^4 + \frac{b_i}{3}E_{11}^3 + \frac{c_i}{2}E_{11}^2 + d_i E_{11}, \tag{3.3}$$

where $d_i = 0$ in all cases. For the connecting layer Ω_3, the Neo-Hookean stored energy is:

$$\psi_3 = \frac{\mu}{2}(I_C - 3) - \mu \ln(J) + \frac{\lambda}{2}(\ln J)^2, \tag{3.4}$$

where μ and λ are Lamé parameters, $I_C = \operatorname{tr}(\boldsymbol{C})$ is the first invariant of the right Cauchy–Green tensor $\boldsymbol{C} = \boldsymbol{F}^\top \boldsymbol{F}$, and $J = \det(\boldsymbol{F})$ with $\boldsymbol{F}$ the deformation gradient. The First Piola-Kirchhoff stress in each domain is:

$$\boldsymbol{P}\big|_{\boldsymbol{x}\in\Omega_i} = \frac{\partial \psi_i}{\partial \boldsymbol{F}}. \tag{3.5}$$

The reaction force on the loading surface is computed by integrating the traction over $\partial\Omega_1$, where $\hat{\boldsymbol{n}}$ denotes the outward unit normal to the surface and $\hat{\boldsymbol{N}}$ denotes the unit vector in the prescribed loading direction. The scalar reaction force in the direction $\hat{\boldsymbol{N}}$ reads:

$$f = \hat{\boldsymbol{N}} \cdot \int_{\partial\Omega_1} \boldsymbol{P}|_{\boldsymbol{u}=\delta\hat{\boldsymbol{n}}} \cdot \hat{\boldsymbol{n}} \ \mathrm{d}A, \tag{3.6}$$

where δ is the prescribed displacement magnitude (so that $\boldsymbol{u} = \delta\hat{\boldsymbol{n}}$ on $\partial\Omega_1$).

b. Single-surface optimization. The target force-displacement curve $\hat{f}(\delta)$ is discretized into T displacement-force pairs $\{(\delta_j, \hat{f}_j),\, j = 1, \ldots, T\}$. The optimization minimizes the squared mismatch between the surrogate force and the target:

$$\mathcal{L} = \frac{1}{2} \sum_j \left(\hat{f}(\delta_j) - \hat{\boldsymbol{N}} \cdot \int_{\partial\Omega_1} \boldsymbol{P}|_{\boldsymbol{u}=\delta_j\hat{\boldsymbol{n}}} \cdot \hat{\boldsymbol{n}} \ \mathrm{d}A \right)^2, \tag{3.7}$$

over the polynomial coefficients a_i, b_i, c_i for each unit cell $i = 1, \ldots, N{\times}M$. In the $2{\times}1$ example, each unit cell contributes three decision variables, giving six in total.

To ensure that the optimized coefficients correspond to designs within the finite element dataset, we apply a barrier penalty. Let $p_1(\delta)$ and $p_2(\delta)$ denote the lower and upper envelopes of the dataset forces at displacement δ. We require, for each unit cell k and each displacement step j:

$$p_1(\delta_j) < f_k(\boldsymbol{u}_j) < p_2(\delta_j). \tag{3.8}$$

To penalize solutions that approach the dataset boundaries, we add a power-law barrier term to the objective. Define the proximity to each bound as

$$r_k^{(1)}(\delta_j) = f_k(\boldsymbol{u}_j) - p_1(\delta_j) - \epsilon_1, \qquad r_k^{(2)}(\delta_j) = p_2(\delta_j) - f_k(\boldsymbol{u}_j) - \epsilon_2, \tag{3.9}$$

where $\epsilon_1, \epsilon_2 > 0$ are small offsets that set a buffer inside the dataset envelope, so that the barrier activates before the hard boundary is reached. Both quantities are positive whenever the constraint $p_1(\delta_j) < f_k(\boldsymbol{u}_j) < p_2(\delta_j)$ is satisfied, and they approach zero as f_k approaches the respective bound. The full objective with barrier terms becomes:

$$\mathcal{L} = \frac{1}{2} \sum_j \left(\hat{f}(\delta_j) - \hat{\boldsymbol{N}} \cdot \int_{\partial\Omega_1} \boldsymbol{P}|_{\boldsymbol{u}=\delta_j\hat{\boldsymbol{n}}} \cdot \hat{\boldsymbol{n}} \ \mathrm{d}A \right)^2 + \gamma \sum_k \sum_j \left(\frac{1}{\left(r_k^{(1)}(\delta_j)\right)^p} + \frac{1}{\left(r_k^{(2)}(\delta_j)\right)^p} \right), \tag{3.10}$$

where $\gamma \geq 0$ is a penalty weight and $p > 0$ controls the steepness of the repulsion near the dataset boundaries. A sufficiently large p approximates a hard wall. This strategy reduces the sensitivity of the result to the initial guess, which is significant in this nonlinear problem. Figure 5 shows the single-surface optimization results for two metamaterial configurations and two desired curve shapes each. For a $1{\times}3$ configuration, the optimized surrogate response follows the objective across the full displacement range. For a $2{\times}2$ configuration, a discrepancy grows with displacement. This discrepancy arises because the surrogate treats unit cells independently and does not capture the mechanical interaction that develops between rows in a fully assembled structure. As the number of rows increases, localized row-to-row interactions become more pronounced. It establishes the foundational force-displacement characteristics of multi-row structures, providing an effective baseline for the inverse design method.

c. Multi-surface optimization. The framework extends to multiple loading surfaces by including one boundary condition and one objective curve per surface. Figure 6 shows a $2{\times}5$ metamaterial with two independent loading surfaces Ω_1 and Ω_2 applied at different locations on the top boundary. The governing equations become:

$$-\operatorname{div}\big(\boldsymbol{P}(\nabla\boldsymbol{u})\big) = \boldsymbol{0} \quad \text{in } \Omega, \tag{3.11}$$

$$\boldsymbol{u}_1 = \boldsymbol{u}_{1,j} \quad \text{on } \partial\Omega_1, \tag{3.12}$$

$$\boldsymbol{u}_2 = \boldsymbol{u}_{2,j} \quad \text{on } \partial\Omega_2, \tag{3.13}$$

$$\boldsymbol{u} = \boldsymbol{0} \quad \text{on } \partial\Omega_{\text{bottom}}. \tag{3.14}$$

The objective now sums the mismatch at both surfaces:

$$\mathcal{L} = \frac{1}{2} \sum_j \left[\left(\hat{f}_1(\delta_{1,j}) - \hat{\boldsymbol{N}} \cdot \int_{\partial\Omega_1} \boldsymbol{P}|_{\boldsymbol{u}_1=\delta_{1,j}\hat{\boldsymbol{n}}} \cdot \hat{\boldsymbol{n}} \ \mathrm{d}A \right)^2 + \left(\hat{f}_2(\delta_{2,j}) - \hat{\boldsymbol{N}} \cdot \int_{\partial\Omega_2} \boldsymbol{P}|_{\boldsymbol{u}_2=\delta_{2,j}\hat{\boldsymbol{n}}} \cdot \hat{\boldsymbol{n}} \ \mathrm{d}A \right)^2 \right], \tag{3.15}$$

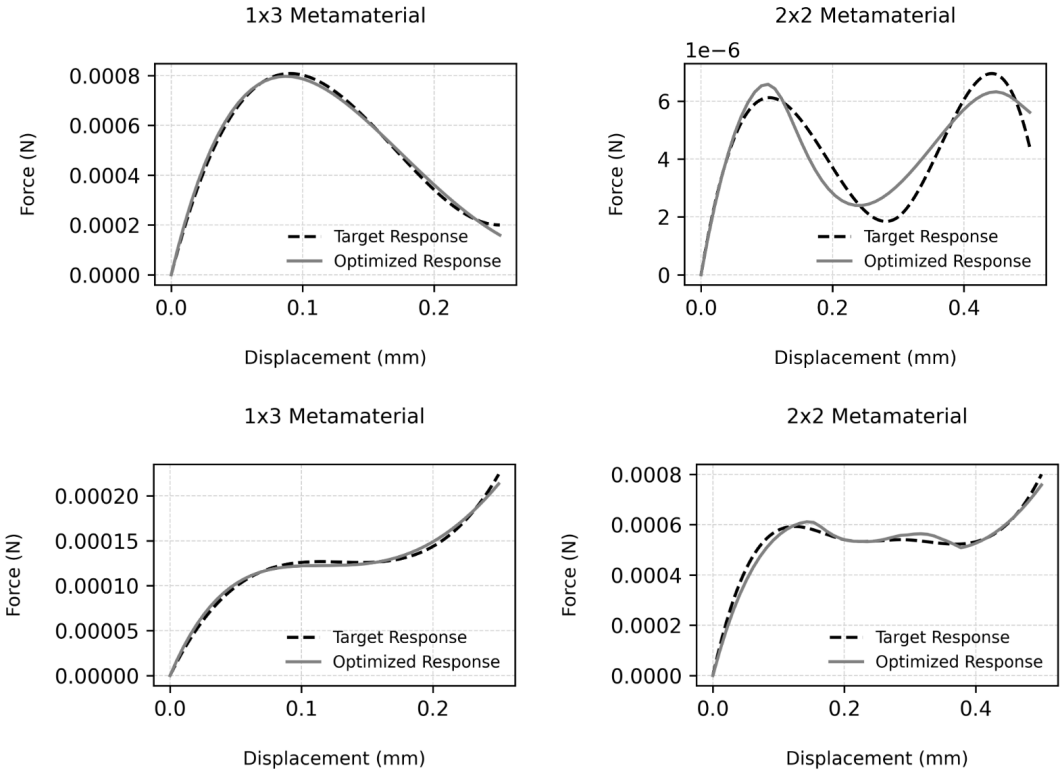

Figure 5. **Surrogate optimization results for single-surface loading.** Each panel compares the desired force-displacement curve (dashed) with the surrogate force at the optimized polynomial coefficients (solid). Results are shown for a 1×3 configuration (left) and a 2×2 configuration (right), each for two different desired shapes. For the single-row configuration, agreement is close across the full displacement range.

where $\hat{f}_1$ and $\hat{f}_2$ are the two desired curves for each surface.

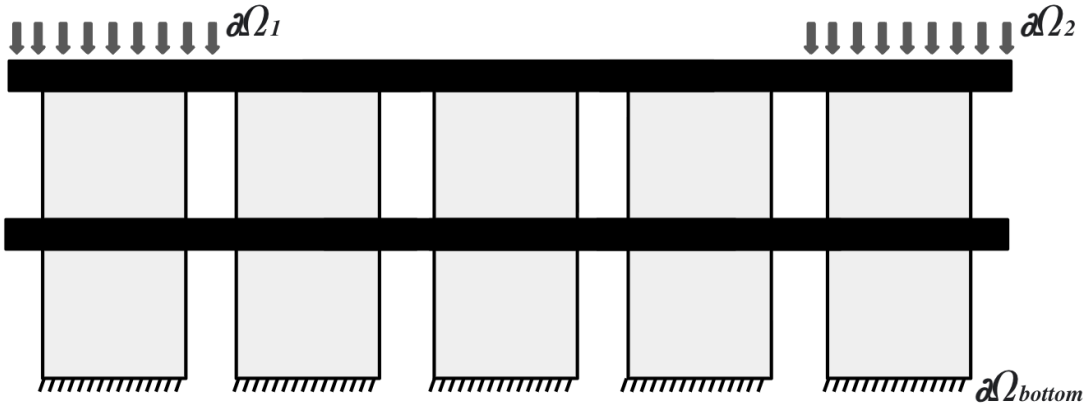

Figure 6. **Multi-surface loading configuration.** A 2×5 metamaterial with two distinct loading surfaces, $\partial\Omega_1$ (top left) and $\partial\Omega_2$ (top right), each subjected to an independent prescribed displacement. The bottom surface is fixed. Each surface can be assigned a different desired force-displacement curve, so that distinct mechanical behaviors are encoded in different regions of a single continuous structure.

Figure 7 shows the result of the multi-surface optimization. The optimized polynomial coefficients bring the response of both loading surfaces close to their respective objectives. The two resulting curves are qualitatively different: one exhibits a stiffening response and the other a plateau followed by a gradual rise. This confirms that the multi-surface formulation can encode spatially distinct mechanical behaviors within a single continuous body without physically separating the two regions.

A notable limitation of the current optimization framework, particularly in multi-row configurations, is its sensitivity to the initial guess. The design space for these highly nonlinear mechanical responses is complex; thus, an ill-chosen starting point can degrade the performance of the optimization algorithm. For instance, attempting to optimize for a constant-force behavior

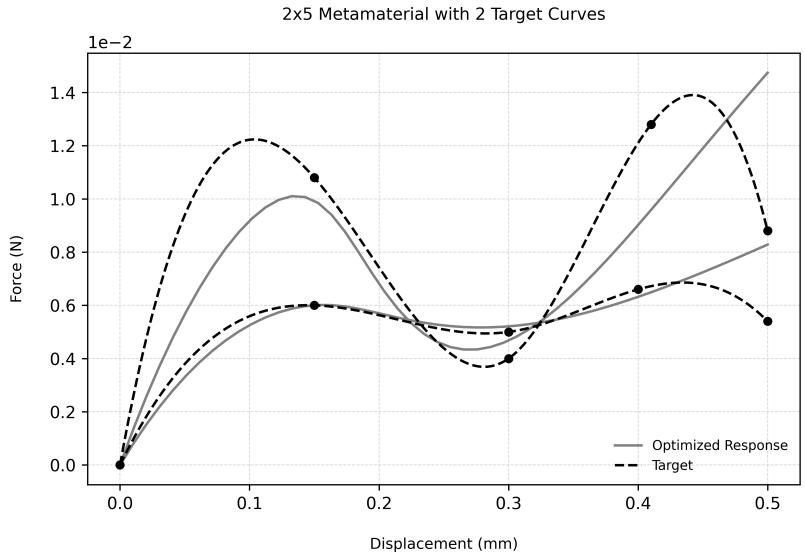

Figure 7. **Multi-surface optimization result for a 2×5 metamaterial.** The optimized force-displacement response (solid) is shown alongside both desired curves (dashed). The surrogate identifies polynomial coefficients for each unit cell such that the response at both loading surfaces matches its respective target. The two curves are qualitatively distinct, confirming that the multi-surface formulation can encode different mechanical behaviors in different regions of a single continuous material.

while initializing the solver with parameters that yield a superelastic response forces the algorithm to navigate across disparate behavioral regimes, often leading to poor convergence. Providing a more informed, physics-guided initial guess would likely mitigate this issue and yield improved optimization outcomes.

3.B. Machine Learning for Shape Parameter Recovery

The surrogate optimization yields the coefficients of the polynomials that approximate the unit cell force-displacement response. This response is represented by a sequence of 50 displacement-force pairs, specifying the mechanical behavior that the cell must produce. The remaining step is to find the eleven shape parameters that generate this response in a finite element simulation. There is no closed-form expression relating shape to response, and the mapping is generally many-to-one: multiple geometries can produce curves that are close to one another. We approach this as a regression problem and solve it with a multi-output multilayer perceptron (MLP) trained on a dataset of 10,295 simulations.

a. Feature representation. Presenting the raw 50 force values directly to the network is possible but not the most informative input representation. We instead map each force-displacement curve to an 82-dimensional feature vector before passing it to the network. The feature vector contains four classes of information. Statistical descriptors capture the mean, variance, skewness, and higher moments of the force signal. Spectral descriptors contain Fourier coefficients that represent the frequency content of the curve. Gradient information provides the local slope at each displacement step, encoding how rapidly force changes with displacement. Energy distribution quantities give the cumulative integral of force up to each displacement point, so that the feature vector carries information about how energy absorption builds over the loading cycle. This representation removes redundancy in the raw signal, emphasizes quantities that vary systematically with geometry, and produces a better-conditioned regression problem than the raw force values.

b. Network architecture and training. The task is to learn the mapping $\hat{\mathbf{x}} = f(\phi(\mathcal{D}))$, where

$$\mathcal{D} = \big\{(\delta_i,\, F_i) \;\big|\; i = 1, 2, \ldots, 50\big\} \tag{3.16}$$

is the specified force-displacement curve, ϕ is the feature extraction operator defined above, $\mathbf{x} = [x_1, \ldots, x_{11}]$ is the shape parameter vector, and f is the regression function to be learned. The network has three hidden layers of sizes $(256, 128, 64)$ with ReLU activations and outputs all eleven shape parameters jointly. Training all output dimensions together allows the network to use correlations between shape parameters: in designs with a particular mechanical character, certain height and width parameters tend to take coordinated values, and joint training captures these dependencies more effectively than training eleven separate single-output models would. Overfitting is controlled by early stopping based on performance on a held-out validation set.

c. Prediction accuracy. Figure 8 compares specified force-displacement curves with curves obtained by running finite element simulations of the geometries predicted by the network, for eight representative examples. The examples span the range of shapes in the dataset: rising responses, curves with a pronounced peak followed by a drop, and curves that remain constant over a range of displacement before rising again. In the examples, the simulation of the predicted geometry follows the target closely. The largest deviations occur near sharp peaks and inflection points, where small changes in shape parameters produce relatively large changes in the force response, making these regions the most demanding for the regression model. Averaged over the full test set, the R^2 between the target and the finite element simulation of the predicted geometry is 0.996.

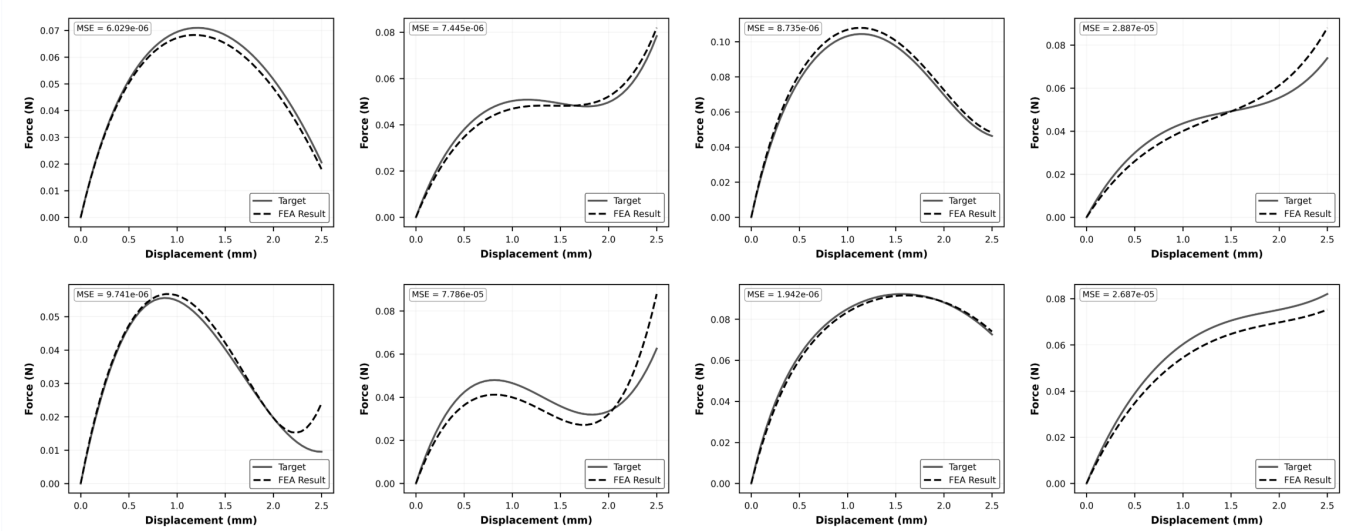

Figure 8. **Machine learning predictions verified by finite element simulation.** Each panel shows an intended force-displacement curve (solid) and the curve produced by simulating the geometry predicted by the network (dashed, labeled FEA Result). Eight representative examples are shown, covering the range of curve shapes in the dataset. The mean squared error (MSE) between target and finite element result is reported in each panel. Agreement is close for most examples; the largest deviations occur near sharp peaks, where the geometry-to-response mapping is most sensitive to small changes in shape parameters.

4. Fabrication and Experimental Comparison

The inverse design approach terminates with a set of eleven shape parameters for each unit cell in the assembled metamaterial. Validating that these parameters produce physically accurate designs requires comparing simulated force-displacement predictions against measurements on fabricated specimens. We therefore fabricated unit cell designs spanning the full behavioral range of the pipeline and subjected each to compression tests.

4.A. Fabricated Designs

A selected set of designs exercises the qualitatively distinct regimes accessible within the fixed topology, spanning bistable designs with varying energy absorption, constant-force behavior, and superelastic designs with different peak forces. These physical prototypes were fabricated by fused deposition modeling in TPU 95A, a thermoplastic polyurethane whose rate-independent elastic behavior is well approximated by the Neo-Hookean constitutive model used in the simulations.

4.B. Mechanical Testing

Compression testing for the fabricated cells was performed on a Mark-10 ESM303 motorized testing machine equipped with a 50 N load cell. Displacement was applied consistently with the rate-independent assumptions underlying the finite element model. Force-displacement curves were recorded continuously over the full prescribed displacement range and stored for comparison with the finite element predictions obtained from the shape parameters returned by the machine learning model.

4.C. Results

Figure 9 illustrates the force-displacement response of a fabricated unit cell under prescribed displacement. The measured experimental curve tracks the finite element prediction closely across the full displacement range, successfully capturing the highly nonlinear structural behavior. The inset photographs correlate key points on the curve with physical deformation states: the initial undeformed geometry, the onset of snap-through instability at the local peak force, and the highly deformed configuration at the local force minimum prior to structural stiffening. Figure 10 presents the complete experimental comparison for the designs. The

superelastic designs exhibit smooth, monotonically rising force-displacement responses in both measurement and simulation. The constant-force design maintains a near-flat force plateau over the tailored displacement range. Both bistable designs exhibit snap-through instability in the experimental response. The critical snap-through force and the post-snap equilibrium force level agree closely with the finite element predictions in both cases. One of the two bistable designs shows a small deviation on the unloading branch, which we attribute to geometric imperfections introduced during printing. Such imperfections perturb the height of the energy barrier between stable states without substantially altering the loading path, producing the asymmetry between loading and unloading branches observed in the measurement. Across all designs and all behavioral regimes, the fabricated specimens reproduce the qualitative character of the predicted responses and agree quantitatively at a level consistent with manufacturing tolerances and the idealization of the constitutive model. To quantitatively evaluate the discrepancy between the physical measurements and the computational predictions, the mean squared error (MSE) is calculated by linearly interpolating the simulated force data onto the discrete experimental displacement coordinates, expressed as $\text{MSE} = \frac{1}{T}\sum_{i=1}^{T}\left[F_{\text{exp}}(\delta_i) - \tilde{F}_{\text{FEA}}(\delta_i)\right]^2$, where $\tilde{F}_{\text{FEA}}$ denotes the calculated numerical force. The mean squared errors reported in Figure 10 confirm that no single behavioral regime presents a systematic failure of the framework; the largest absolute errors occur in the bistable designs, where the steep force drop at snap-through amplifies the sensitivity of the error metric to small displacement shifts in the instability point.

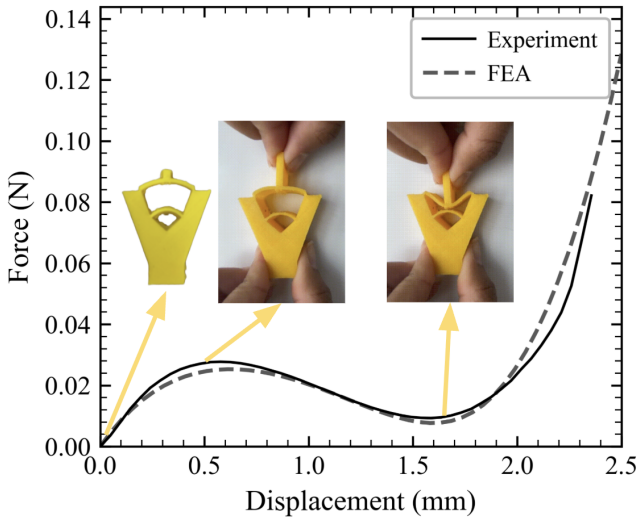

Figure 9. **Force-displacement response and deformation stages of a representative unit cell.** The experimental measurement (solid line) shows agreement with the finite element prediction (dashed line). Inset photographs illustrate the physical deformation at key points along the response curve: the initial undeformed state (left), the onset of snap-through instability near the local peak force (middle), and the highly deformed buckled configuration at the local force minimum (right).

5. Conclusions and Future Work

We have presented a two-scale inverse design methodology for mechanical metamaterials that extends previous work in two ways. First, the pipeline targets the force-displacement response of the assembled metamaterial rather than individual unit cells in isolation, using a polynomial surrogate model at the metamaterial scale to connect unit cell behavior to the macroscale response. Second, the framework handles multiple independent loading surfaces within a single continuous structure, allowing different regions of the same metamaterial to produce qualitatively distinct force-displacement behaviors simultaneously. This design method is particularly advantageous for metamaterials characterized by complicated unit cells, where the nonlinear mapping between the unit cell geometry and the response of the metamaterial is computationally expensive. By employing a surrogate model, navigating these intricate design spaces to obtain targeted mechanical responses becomes significantly more tractable and efficient. The process combines three components. A polynomial surrogate model replaces each unit cell with a rectangular domain governed by a polynomial energy density whose derivative yields a third-order constitutive response and optimizes the coefficients of each domain to minimize the mismatch between the assembled surrogate response and the prescribed target. A finite element dataset of 10,295 simulations maps the eleven-parameter shape space to force-displacement curves. A multilayer perceptron trained on this dataset inverts the geometry-to-response mapping at the unit cell scale, recovering the shape parameters that produce any desired curve the surrogate optimizer specifies. Fabricated prototypes in TPU 95A confirm that the system produces designs whose physical responses agree with predictions across superelastic, constant-force, and bistable behaviors.

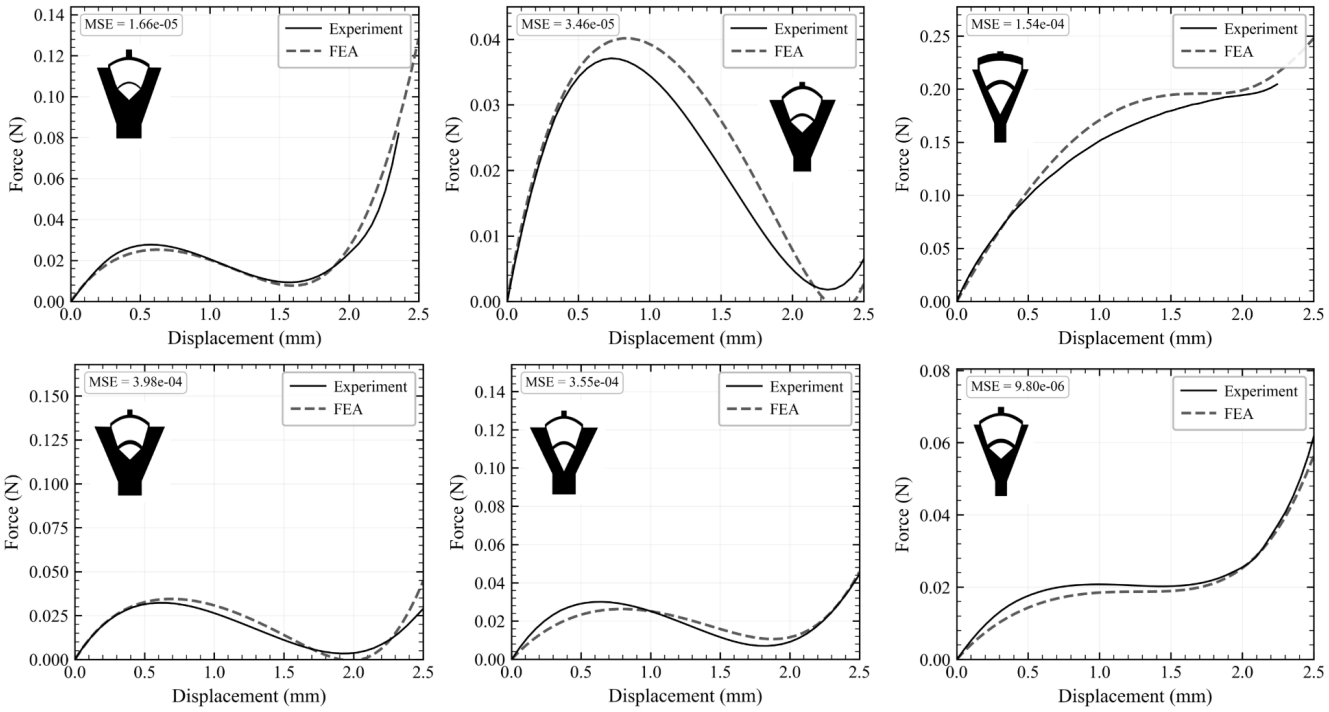

Figure 10. **Measured force-displacement curves compared with finite element predictions for six fabricated designs.** In each panel, the solid curve is the experimental measurement and the dashed curve is the finite element prediction obtained from the shape parameters returned by the machine learning model; the mean squared error (MSE) between the two is reported in each panel inset. The unit cell geometry is shown alongside each panel. The six designs span the full behavioral range intended by the process: superelastic responses at different peak forces, constant-force response, and bistable responses with different levels of energy absorption.

Several aspects of the current framework can be developed further. The polynomial surrogate model treats unit cells independently. For single-row metamaterials this approximation performs well, but for multi-row configurations the coupling between adjacent rows introduces discrepancies that grow with the number of rows. Incorporating row-to-row interactions in the surrogate, either through a more detailed constitutive description of the interface regions or through a formulation that treats groups of cells as a unit, would reduce this error. The machine learning model's accuracy depends on how well the training data covers the region of shape space relevant to a given required curve. The current dataset samples the eleven parameters broadly, but coverage near transitions between behavioral regimes, such as the boundary between superelastic and bistable responses, is not specifically dense. Targeted data collection in these regions, guided by active learning or by the distribution of targets produced during optimization, would improve accuracy where it is most important. The framework is specific to the planar topology explored here. Applying it to three-dimensional topologies or to topologies with different connectivity would require new simulation data and retraining the machine learning model, but the structure of the process would carry over directly. Three-dimensional topologies would give access to anisotropic responses and multi-axial loading scenarios that are not reachable within a planar geometry. The multi-surface results suggest a path toward spatially graded metamaterials in which every unit cell is independently optimized for its local loading environment. In the prosthetics application that motivated this work, this would mean specifying the desired energy absorption at the socket tip, the gripping force profile along the lateral walls, and the stiffness transition between them in a single design pass, with the methodology determining the full spatial distribution of unit cell geometries. Extending the framework to loading conditions that vary with direction or rate would broaden its range of application to structures whose mechanical environment changes both in space and over time. Finally, as a direct extension of this work, future efforts will focus on the physical fabrication and comprehensive experimental testing of these computationally optimized metamaterial structures. Validating the numerically predicted behaviors of complex, multi-row designs against physical prototypes under realistic loading conditions will be crucial to establish the practical efficacy of the proposed inverse design methodology.

Acknowledgments

We acknowledge ARO (MURI W911NF-24-2-0184) and a fellowship from Carnegie Mellon University's Center for Machine Learning and Health. The authors gratefully acknowledge Professor Levent Burak Kara for his valuable discussions and insights,

as well as the undergraduate students Miguel Brandao, Siya Scindia, and Summer Sun for their contributions to this work.

[BVCVH17] Katia Bertoldi, Vincenzo Vitelli, Johan Christensen, and Martin Van Hecke. Flexible mechanical metamaterials. *Nature Reviews Materials*, 2(11):1–11, 2017.

[dSDC] Francesco dell'Isola, David Steigmann, and Alessandro Della Corte. Synthesis of complex structures. designing micro-structure to deliver targeted macro-scale.

[DZD+22] Bolei Deng, Ahmad Zareei, Xiaoxiao Ding, James C Weaver, Chris H Rycroft, and Katia Bertoldi. Inverse design of mechanical metamaterials with target nonlinear response via a neural accelerated evolution strategy. *Advanced Materials*, 34(41):2206238, 2022.

[FCvH14] Bastiaan Florijn, Corentin Coulais, and Martin van Hecke. Programmable mechanical metamaterials. *Physical review letters*, 113(17):175503, 2014.

[FFK+16] Tobias Frenzel, Claudio Findeisen, Muamer Kadic, Peter Gumbsch, and Martin Wegener. Tailored buckling microlattices as reusable light-weight shock absorbers. *Advanced materials (Deerfield Beach, Fla.)*, 28(28):5865–5870, 2016.

[FWC+22] Xin Fang, Jihong Wen, Li Cheng, Dianlong Yu, Hongjia Zhang, and Peter Gumbsch. Programmable gear-based mechanical metamaterials. *Nature Materials*, 21(8):869–876, 2022.

[HLP18] Chan Soo Ha, Roderic S Lakes, and Michael E Plesha. Design, fabrication, and analysis of lattice exhibiting energy absorption via snap-through behavior. *Materials & Design*, 141:426–437, 2018.

[HSSP+16] Babak Haghpanah, Ladan Salari-Sharif, Peyman Pourrajab, Jonathan Hopkins, and Lorenzo Valdevit. Multistable shape-reconfigurable architected materials. *Adv. Mater*, 28(36):7915–7920, 2016.

[HWL+23] Zhengtong Han, Kai Wei, Xiaoyang Liu, Yuhang Long, Jialong Li, and Xinglin Chen. Developing mechanical metamaterials under an adaptable topology optimization design framework. *Acta Mechanica Solida Sinica*, 36(2):306–316, 2023.

[HYX+23] Chan Soo Ha, Desheng Yao, Zhenpeng Xu, Chenang Liu, Han Liu, Daniel Elkins, Matthew Kile, Vikram Deshpande, Zhenyu Kong, Mathieu Bauchy, et al. Rapid inverse design of metamaterials based on prescribed mechanical behavior through machine learning. *Nature Communications*, 14(1):5765, 2023.

[IFW+16] Alexandra Ion, Johannes Frohnhofen, Ludwig Wall, Robert Kovacs, Mirela Alistar, Jack Lindsay, Pedro Lopes, Hsiang-Ting Chen, and Patrick Baudisch. Metamaterial mechanisms. In *Proceedings of the 29th annual symposium on user interface software and technology*, pages 529–539, 2016.

[JMR+23] Pengcheng Jiao, Jochen Mueller, Jordan R Raney, Xiaoyu Zheng, and Amir H Alavi. Mechanical metamaterials and beyond. *Nature communications*, 14(1):6004, 2023.

[KSK+24] Sukheon Kang, Hyunggwi Song, Hyun Seok Kang, Byeong-Soo Bae, and Seunghwa Ryu. Customizable metamaterial design for desired strain-dependent poisson's ratio using constrained generative inverse design network, Nov 2024.

[KZ17] H MA Kolken and AA Zadpoor. Auxetic mechanical metamaterials. *RSC advances*, 7(9):5111–5129, 2017.

[LMW12] Anders Logg, Kent-Andre Mardal, and Garth Wells. *Automated solution of differential equations by the finite element method: The FEniCS book*, volume 84. Springer Science & Business Media, 2012.

[MJS+18] Mohammad J Mirzaali, Shahram Janbaz, M Strano, L Vergani, and Amir A Zadpoor. Shape-matching soft mechanical metamaterials. *Scientific reports*, 8(1):965, 2018.

[MPQF16] Andrew G Mark, Stefano Palagi, Tian Qiu, and Peer Fischer. Auxetic metamaterial simplifies soft robot design. In *2016 IEEE international conference on robotics and automation (ICRA)*, pages 4951–4956. Ieee, 2016.

[PMV15] Jayson Paulose, Anne S Meeussen, and Vincenzo Vitelli. Selective buckling via states of self-stress in topological metamaterials. *Proceedings of the National Academy of Sciences*, 112(25):7639–7644, 2015.

[PRGM21] Aniket Pal, Vanessa Restrepo, Debkalpa Goswami, and Ramses V Martinez. Exploiting mechanical instabilities in soft robotics: Control, sensing, and actuation. *Advanced Materials*, 33(19):2006939, 2021.

[RBS19] Ahmad Rafsanjani, Katia Bertoldi, and André R Studart. Programming soft robots with flexible mechanical metamaterials. *Science Robotics*, 4(29):eaav7874, 2019.

[SGD+19] James Utama Surjadi, Libo Gao, Huifeng Du, Xiang Li, Xiang Xiong, Nicholas Xuanlai Fang, and Yang Lu. Mechanical metamaterials and their engineering applications. *Advanced Engineering Materials*, 21(3):1800864, 2019.

[Sig09] Ole Sigmund. Systematic design of metamaterials by topology optimization. In *IUTAM Symposium on Modelling Nanomaterials and Nanosystems: Proceedings of the IUTAM Symposium held in Aalborg, Denmark, 19–22 May 2008*, pages 151–159. Springer, 2009.

[SKR+15] Sicong Shan, Sung H Kang, Jordan R Raney, Pai Wang, Lichen Fang, Francisco Candido, Jennifer A Lewis, and Katia Bertoldi. Multistable architected materials for trapping elastic strain energy. *Adv. Mater*, 27(29):4296–4301, 2015.

[SM23] P Sinha and T Mukhopadhyay. Programmable multi-physical mechanics of mechanical metamaterials. *Materials Science and Engineering: R: Reports*, 155:100745, 2023.

[WWC+21] Lingling Wu, Yong Wang, Kuochih Chuang, Fugen Wu, Qianxuan Wang, Weiqi Lin, and Hanqing Jiang. A brief review of dynamic mechanical metamaterials for mechanical energy manipulation. *Materials Today*, 44:168–193, 2021.

[YCZ19] Shangqin Yuan, Chee Kai Chua, and Kun Zhou. 3d-printed mechanical metamaterials with high energy absorption. *Advanced Materials Technologies*, 4(3):1800419, 2019.

[YM19] Hang Yang and Li Ma. Multi-stable mechanical metamaterials by elastic buckling instability. *Journal of materials science*, 54(4):3509–3526, 2019.

[ZDZ+23] Qingliang Zeng, Shengyu Duan, Zeang Zhao, Panding Wang, and Hongshuai Lei. Inverse design of energy-absorbing metamaterials by topology optimization. *Advanced Science*, 10(4):2204977, 2023.

[ZVLR+21] Yunlan Zhang, Mirian Velay-Lizancos, David Restrepo, Nilesh D Mankame, and Pablo D Zavattieri. Architected material analogs for shape memory alloys. *Matter*, 4(6):1990–2012, 2021.

[ZZCW23] Xiaoyang Zheng, Xubo Zhang, Ta-Te Chen, and Ikumu Watanabe. Deep learning in mechanical metamaterials: From prediction and generation to inverse design. *Advanced Materials*, 35(45), Nov 2023.

[ZZLW23] Qingliang Zeng, Zeang Zhao, Hongshuai Lei, and Panding Wang. A deep learning approach for inverse design of gradient mechanical metamaterials. *International Journal of Mechanical Sciences*, 240:107920, 2023.